

Iron doped manganese cobaltite spinel coatings produced by electrophoretic co-deposition on interconnects for solid oxide cells: Microstructural and electrical characterization

*Original*

Iron doped manganese cobaltite spinel coatings produced by electrophoretic co-deposition on interconnects for solid oxide cells: Microstructural and electrical characterization / Zanchi, E.; Molin, S.; Sabato, A. G.; Talic, B.; Cempura, G.; Boccaccini, A. R.; Smeacetto, F.. - In: JOURNAL OF POWER SOURCES. - ISSN 0378-7753. - ELETTRONICO. - 455:(2020), p. 227910. [10.1016/j.jpowsour.2020.227910]

*Availability:*

This version is available at: 11583/2805018 since: 2020-03-21T00:57:34Z

*Publisher:*

Elsevier B.V.

*Published*

DOI:10.1016/j.jpowsour.2020.227910

*Terms of use:*

This article is made available under terms and conditions as specified in the corresponding bibliographic description in the repository

*Publisher copyright*

Elsevier postprint/Author's Accepted Manuscript

© 2020. This manuscript version is made available under the CC-BY-NC-ND 4.0 license  
<http://creativecommons.org/licenses/by-nc-nd/4.0/>. The final authenticated version is available online at:  
<http://dx.doi.org/10.1016/j.jpowsour.2020.227910>

(Article begins on next page)

# **Iron doped manganese cobaltite spinel coatings produced by electrophoretic co-deposition on interconnects for solid oxide cells: microstructural and electrical characterization**

E. Zanchi <sup>1</sup>, S. Molin <sup>2</sup>, A. G. Sabato <sup>1</sup>, B. Talic <sup>3</sup>, G. Cempura <sup>4</sup>, A. R. Boccaccini <sup>5</sup>, F. Smeacetto<sup>1\*</sup>

<sup>1</sup> Department of Applied Science and Technology, Politecnico di Torino, Corso Duca degli Abruzzi 24, 10129  
Torino, Italy

<sup>2</sup> Faculty of Electronics, Telecommunications and Informatics, Gdańsk University of Technology, ul.  
Narutowicza 11/12, 80-233 Gdańsk, Poland

<sup>3</sup> Department of Energy Conversion and Storage, Technical University of Denmark, DTU Risø Campus,  
Frederiksborgvej 399, DK-4000 Roskilde, Denmark

<sup>4</sup> AGH University of Science and Technology, al. Mickiewicza 30, 30-059 Krakow, Poland

<sup>5</sup> Department of Materials Science and Engineering, University of Erlangen-Nuremberg, Cauerstr. 6,  
91058 Erlangen, Germany

*Corresponding author:* e-mail [federico.smeacetto@polito.it](mailto:federico.smeacetto@polito.it);

## **Abstract**

We report a systematic microstructural and electrical characterization of iron doped Mn-Co spinel coatings processed by electrophoretic co-deposition of  $\text{Mn}_{1.5}\text{Co}_{1.5}\text{O}_4$  and  $\text{Fe}_2\text{O}_3$  powders on Crofer 22 APU and AISI 441 steel substrates. Iron addition to Mn-Co spinel coating leads to a reduction of the area specific resistance on both substrates, after 3200h at 750°C. The Fe doped Mn-Co coating both leads to a thinner oxide scale and reduces the sub scale oxidation for the Crofer 22 APU substrate. Fe doped Mn-Co on AISI 441 shows both a thicker oxide scale and low area specific resistance values, likely due to a doping effect of the oxide scale by minor alloying elements. The different mechanisms by which iron doping of Mn-Co spinels can influence

elemental interdiffusion at the steel-oxide scale-coating interfaces and relative contributions to the overall area specific resistance are evaluated by means of advanced electron microscopy. The promising results are further confirmed in a cell test, where the Fe doped MnCo coated interconnect does not induce any degradation of the oxygen electrode, proving its efficiency.

**Keywords:** electrophoretic deposition; coating; solid oxide cells; electron microscopy

## 1. Introduction

Chromia-forming ferritic stainless steels (FSSs) are widely employed in planar Solid Oxide Cell (SOC) stacks; special FSSs have been specifically developed as interconnect alloys over the last years [1–3]. The common feature of these steels is the high Cr concentration (>20 %), required to ensure satisfactory corrosion resistance at the SOC operating temperature (500-900 °C [4]).

However, the interconnect performance and the durability of the whole SOC stack (whose typical lifetime target is > 40 000 h) remain affected by two issues. First, the continuous growth of the chromia scale during stack operation progressively reduces the electrical conductivity of the interconnect. Indeed, the conductivity of Cr<sub>2</sub>O<sub>3</sub> ( $0.6\text{--}16 \times 10^{-2} \text{ Scm}^{-1}$  at 800 °C [5]) is more than four orders of magnitude lower than that of the steel. The second issue is related to the formation of volatile Cr-compounds that deposit on the air electrode, degrading the electrochemical performance of the cells [6]. The Cr evaporation rate is partially reduced by introducing 0,3-0,5 wt. % of Mn in the alloy; however, the well adherent Cr-Mn spinel that forms at the top of Cr<sub>2</sub>O<sub>3</sub> scale has been reported to **reduce**, but not completely avoid the cathode poisoning [7,8].

Therefore, various protective coatings have been recently proposed, produced and tested [9]. Among them, the (Mn,Co)<sub>3</sub>O<sub>4</sub> spinel class was shown to be particularly promising due to satisfactory electrical conductivity ( $50\text{--}90 \text{ Scm}^{-1}$  at 800 °C), TEC match with other SOC materials ( $11\text{--}12.5 \times 10^{-6} \text{ K}^{-1}$  [10]) and good adhesion to the steel [11–13]. Furthermore, several studies demonstrated that (Mn,Co)<sub>3</sub>O<sub>4</sub> coatings effectively reduce both chromium evaporation and corrosion degradation of the steel substrate [13–19]. Research is now oriented to further improve the characteristics of the Mn-Co spinel coating by transition metal doping, mainly

Fe and Cu [20–28]. Properties and performance of obtained coatings strongly depend on both the production and deposition methods.

In our previous work [29] we obtained Mn-Co spinel coatings doped with different Fe amounts by electrophoretic co-deposition (EPD) of  $\text{Fe}_2\text{O}_3$  and  $\text{Mn}_{1.5}\text{Co}_{1.5}\text{O}_4$  on Crofer 22 APU. Fe-doped coatings demonstrated a lower parabolic oxidation rate and thinner oxide scale in comparison with both the pristine  $\text{Mn}_{1.5}\text{Co}_{1.5}\text{O}_4$  spinel coating (MCO) and bare Crofer 22 APU after 2000 h aging at 750°C. Also Bednarz et al. [27] concluded that Fe-modified MCO coatings exhibit an improved high-temperature oxidation resistance compared to the unmodified MCO coating.

In terms of electrical properties, both Masi et al. [23] and Talic et al. [22] have shown that Fe-doped Mn-Co spinels exhibit a lower electrical conductivity compared to the undoped spinel. This is related to the fact that  $\text{Fe}^{3+}$  cations preferentially occupy the octahedral sites of the spinel structure, causing both an increase of the lattice parameter and a reduction on the probability of polaron hopping between adjacent sites of the spinel lattice [30]. However, the mechanism by which Fe-doping of Mn-Co spinels can influence elements inter-diffusion at the FSS-oxide scale-coating interfaces and relative contributions to the overall electrical resistance of different FSS interconnects has not been clearly established.

The present paper extends our previous study on Fe-doped MCO spinel and seeks to examine the contribution of Fe-addition to the overall electrical resistance of FSS interconnects, in comparison with undoped MCO coated substrates. In particular, we focus on the characterization of  $\text{Mn}_{1.35}\text{Co}_{1.35}\text{Fe}_{0.30}\text{O}_4$  coated steel, since this coating has already demonstrated the best performance in terms of oxidation kinetics and stability at high-temperature, due to both a controlled level of Fe-doping and a two-step sintering.

Long-term area specific resistance has been evaluated for two different coated FFS substrates: the special alloy Crofer 22 APU and the commercial-grade AISI 441. A comprehensive post-mortem characterization has been carried out, highlighting phenomena occurring at different interfaces during tests at 750°C and the influence of alloys compositions is discussed by making use of advanced microscopy techniques.

## 2. Experimental

### 2.1 Sample preparation

Two different steels were used as substrates for coating deposition: Crofer 22 APU (Thyssen Krupp, Cr=23 wt. %, Mn=0.5 wt. %, La= 0.1 wt. %, Ti<0.1 wt. %, Si and Al <0.05 wt. %, Fe=Bal.) and AISI 441 (Cr=17.5 wt. %, Mn=0.4 wt. %, Si=0.6 wt. %, Nb= 0.4 wt. %, Ti=0.2 wt. %, Ni= 0.1 wt. %, Al <0.1 wt. %, Fe=Bal.). For ASR test, 20 × 60 mm coupons were cut from steel plates (0.3 mm thick) and Ø6 mm holes were punched on both shorter sides. The steel coupons were ground with SiC paper and diamond abrasive to remove residual oxides. After cleaning the coupons in ultrasonic bath (10 min in acetone and 10 min in ethanol), platinum wires (0,3 mm diameter) were flattened and welded at the shorter edge of each of them.

Commercially available  $\text{Mn}_{1.5}\text{Co}_{1.5}\text{O}_4$  spinel powder (Fuelcellmaterials,  $d_{50}=634$  nm) and  $\text{Fe}_2\text{O}_3$  powder (Fluka,  $d_{50}=75$  nm) were chosen for the electrophoretic co-deposition. EPD suspensions were prepared dispersing oxide powders in ethanol and deionised water (60/40 vol.%) solution. The concentration of solids was fixed at  $37.5 \text{ gL}^{-1}$ . In order to coat both surfaces of steel substrates, EPD was performed by a three-electrode setup; deposition voltage was fixed at 50 V and applied for 20 s. More details about the EPD process and the co-deposition mechanism of MCO and  $\text{Fe}_2\text{O}_3$  are reported in our previous work [29]. Two suspensions were prepared in this case: MCO (100 wt. %  $\text{Mn}_{1.5}\text{Co}_{1.5}\text{O}_4$ ), and 10FeMCO (90 wt. %  $\text{Mn}_{1.5}\text{Co}_{1.5}\text{O}_4$ , 10 wt. %  $\text{Fe}_2\text{O}_3$ ).

Coated steel samples were dried at room temperature and then subjected to a two-step sintering. The first treatment was performed in reducing atmosphere ( $\text{Ar}/\text{H}_2$  4 vol. %) for 2 h; temperature was fixed at 900 °C for MCO coated samples and at 1000 °C for Fe-doped samples (in the following labelled 10FeMCO\_R1000). The second step was in oxidizing condition (static air) for 2 h at 900 °C for both undoped and Fe-doped coated samples. The reason for the two different heat treatments for the MCO and Fe doped MCO originate from our previous study [29], where the 1000 °C reducing step was necessary and processed only for the Fe doped MCO.

## 2.2 Area specific resistance measurement

The evaluation of the high-temperature ASR was carried out in a specific measurement rig, already described in previous studies [21,25]. Coated coupons were stacked together and separated from each other by two porous plates ( $20 \times 20 \times 1$  mm) of  $\text{La}_{0.85}\text{Sr}_{0.15}\text{MnO}_3$  (LSM), that was chosen as contact material. The production method for the LSM plates is described in detail elsewhere [25]. ~~Pt wires were placed between the LSM plates; two gold foils were positioned at the bottom and at the top of the stack to provide the electric current. Alumina spacers were used to avoid short circuits among samples. The stack was positioned between alumina blocks; a load of 8 kg was placed at the top to improve the contact area.~~

The temperature of the furnace was set to 750 °C; two thermocouples positioned close to samples ~~(one at the top and one at the bottom of the stack)~~ monitored the temperature ~~(the  $\Delta T$  resulted of 8 °C on average at 750 °C)~~. When 750 °C was reached, a current of 2 A, equal to  $0.5 \text{ Acm}^{-2}$ , was applied. The voltage drop between each pair of Pt wire was measured by an external resistor for 3200 h at a constant temperature. ~~ASR measurements were carried out as following: steel substrates were coated on both sides by EPD deposition method and Pt wires were connected and welded to both side before coating application and sintering. ASR monitoring was reported as the average of the 2 detected voltage drops of the two surfaces.~~ The area specific resistance was calculated according to:

$$ASR = \frac{\Delta V_{int}}{I_{ext}} \times A_{cont} \quad (1)$$

where  $\Delta V_{int}$  is the voltage drop across each interface (up or down) of samples,  $I_{ext}$  is the set current (2 A) and  $A_{cont}$  is the contact area, determined by the LSM plates ( $4 \text{ cm}^2$ ). ~~Considering the specification of the external resistor, the equation (1) can be written:~~

$$ASR = R_{ext} \times \frac{\Delta V_{int}}{V_{ext}} \times A_{cont} \quad (2)$$

~~where  $R_{ext}$  corresponds to  $0.012 \Omega$  and  $V_{ext}$  is overall voltage constantly measured by the external system.~~

After 3200 h at 750°C, the furnace was cooled down; the ASR values recorded during the cooling were used to calculate the activation energy for the electrical conduction. ~~, following the Arrhenius equation:~~

$$\frac{ASR}{T} = Ae^{\left(\frac{E_A}{kT}\right)} \quad (3)$$

where  $A$  is a pre-exponential factor [ $\Omega\text{cm}^{-2}\text{K}^{-1}$ ],  $E_A$  is the activation energy [ $\text{kJ mol}^{-1}$ ],  $k$  is the Boltzmann's constant [ $\text{eV K}^{-1}$ ] and  $T$  is the temperature [K].

The stack was then embedded in epoxy resin (Struers, Denmark), cut to obtain the cross section and polished. Morphological and compositional characterization was performed by scanning electron microscope (SEM, Zeiss Merlin) equipped with an energy dispersive X-Ray analyser (EDX, Bruker). For quantification of the EDX spectra, Esprit 2.0 software from Bruker was used. The porosity of the coatings has been evaluated using the ImageJ software [31] and considering at least four images from different areas of each sample. FIB lamellae for transmission electron microscopy (TEM) analysis were prepared using NEON CrossBeam 40EsB of ZEISS. TEM investigations were performed on high resolution, Titan Cubed G2 60-300 (FEI) - a probe Cs corrected (S)TEM, equipped with ChemiSTEM EDX system based on a four windowless Silicon Drift Detectors (Super X). STEM imaging was performed in high angle annular dark-field (HAADF) mode. Analysis of crystal structure (phase composition) was performed using TEM-SAED method supported by JEMS software.

### 2.3 Fuel cell test

Anode supported fuel cell of 25 mm (produced by Department of Materials and Mineral Resources Engineering, National Taipei University of Technology, Taiwan) was used in fuel cell test. The cell had a NiO-YSZ anode, YSZ electrolyte with CGO barrier layer and a  $1\text{ cm}^2$  LSCF cathode. The cell was sealed to an alumina tube using Aremco 552 ceramic adhesive. Gold mesh was used for current collection from the cathode. For the test of the the influence of the interconnect, Crofer 22 APU steel with 10FeMCO\_R1000 coating was used. Electrophoretic deposition was performed according to the same procedure described in Section 2.1. Sample with approximate dimensions of  $2.5 \times 2.5\text{ cm}^2$  was placed 4 mm next to the cathode (with parallel surfaces) on alumina spacer. Anode was fed with pure  $\text{H}_2$  with a flow rate of 80 sccm, air was delivered to the inside of the furnace (500 sccm). Electrochemical characterization was performed using Solartron 1260 coupled with Solartron 1287. After initial reduction, the cell was tested at  $750\text{ }^\circ\text{C}$  under a current of  $250\text{ mA cm}^{-2}$  for  $\approx 12\text{ h}$  and then at a current of  $500\text{ mA cm}^{-2}$ . Impedance spectra were recorded at OCV and after 45 and 175 hours.

Post mortem analysis of the interconnect and cell was performed using Thermo Fisher Phenom XL electron microscope with energy dispersive x-ray analyser (EDX). Backscattered electrons were used for observation, accelerating voltage was 15 kV. For observation, samples were embedded in epoxy (EpoFix, Struers) and polished down to 1  $\mu\text{m}$  finish.

### 3. Results

#### 3.1 Area specific resistance evaluation

Figure 1 shows the Area Specific Resistance (ASR) of AISI 441 (A) and Crofer 22 APU (B) coated samples measured over 3200 h at 750 °C and under a current density of 0.5  $\text{Acm}^{-2}$ . ~~Since no significant difference between the voltage drops on the two surfaces of each sample was registered the reported ASR values are the average between the two connections for each set of samples.~~

All curves in Figure 1 exhibit an initial decreasing trend of ASR: this can be attributed to LSM sintering and creep which caused an increase of the real contact area [25]. Depending on the sample, the contribution of the LSM sintering is considerable till approximately 1000 h of aging. The jump in ASR visible at around 400 h for the MCO samples was due to thermal adjustment of the furnace (the temperature mismatch between the program and the thermocouples inside the measurement rig was balanced, bringing the real temperature from around 700 to exactly 750 °C).

As summarized in Table 1, ASR values at the end of the test (3200 h) were found to be in the same range ( $24.3 \div 27.8 \text{ m}\Omega \text{ cm}^2$ ) for both undoped and Fe-doped samples. These values are comparable to the ASR of Mn-Co spinel coated FSSs reported in previous studies [17,21,25,32,33]. However, ASR of both AISI 441 and Crofer 22 APU shows that 10FeMCO\_R1000 coating led to a slight reduction of the area specific resistance of about  $2.5 \div 3.5 \text{ m}\Omega \text{ cm}^2$  during the test.

The comparison of Figure 1 A and B reveals that different phenomena involved AISI 441 and Crofer 22 APU coated samples. Indeed, ASR of both MCO and 10FeMCO\_R1000 coatings on AISI 441 (Figure 1 A) reached a steady state after about 1000 h of testing, maintaining an almost constant resistance value till the end of the test. Coated Crofer 22 APU samples (Figure 1 B) exhibited an increasing ASR over time, starting from around



2000 h at 750 °C. In order to quantify this effect, the degradation rates, or  $\Delta\text{ASR}/1000$  h, were calculated by considering the slope of the linear fits to the data between 2000 and 3200 h; results are reported in Table 1.

~~What is interesting in this graph is the higher degradation rate of the 10FeMCO\_R1000-coated Crofer. Despite the increase of ASR, final values of coated Crofer 22 APU differ less than  $1 \text{ m}\Omega \text{ cm}^2$  from coated AISI 441 samples.~~ The temperature dependence of the area specific resistance was determined by recording the ASR of samples during the cooling of the measurement rig; plots are presented in the insets of Figure 1 A and B respectively for the two steel substrates and the activation energies obtained by the slope of the trend lines are reported in Table 1. Values of  $E_A$  range from 0.60 and 0.69 eV and lay in the same order of magnitude of results in literature [19,21,27].

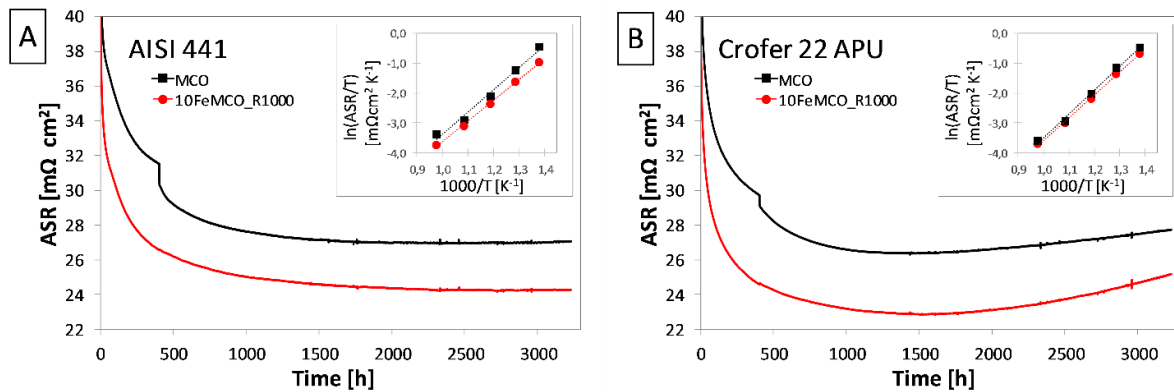


Figure 1: ASR development over time (750 °C, 3200 h, 0.5 Acm<sup>2</sup>) and as a function of temperature for respectively A) AISI 441 and B) Crofer 22 APU coated samples.

	AISI 441		Crofer 22 APU		
	ASR 3200h	EA	ASR 3200h	Lin. Degr. Rate	E <sub>A</sub>
	[mΩ cm <sup>2</sup> ]	[eV]	[mΩ cm <sup>2</sup> ]	[mΩ cm <sup>2</sup> /1000h]	[eV]
MCO	27.0	0.64	27.8	0.92	0.69
10FeMCO_R1000	24.3	0.60	25.2	1.70	0.66

Table 1: ASR after 3200 h at 750 °C. linear degradation rates and activation energies (between 750 and 450°C) of the studied samples.

### 3.2 Microstructure after ASR test

Figure 2 provides FE-SEM pictures collected on the cross-sections of the samples at the end of the ASR test (3200 h, 750 °C, air). Neither delamination nor spallation of the coatings was clearly visible at the end of the

test in any of the measured samples; however the effect of the different substrate on the morphology is evident comparing images of the same coatings deposited on Crofer 22 APU (Figure 2 a and b) and AISI 441 (Figure 2 c and d). In the first case, coatings exhibited a good interface with the substrate after aging. On the other hand, all coated AISI 441 samples exhibited a crack between the steel and the oxide scale; in Figure 2 c the coating is detached from the substrate because of a reaction with the LSM contact layer. The observation is consistent with other publications that reported on the weak interface between the AISI 441 steel and its chromia scale [33,34].

The thermally grown oxide scale of Crofer 22 APU substrate (marked in dashed line in Figure 2 a and b) presents irregular thickness and Mn-rich sub-scale nodules. The nodules are more evident in MCO coated samples, that was subjected to two sintering treatment both at 900 °C. In Figure 2 b the same steel substrate coated by 10FeMCO\_R1000 exhibits both a thinner oxide scale and the absence of visible sub-scale nodules. In particular, measurements on a significant number of EDX line-scans (not reported here) estimate that the thickness of the chromia scale is  $1.4 \pm 0.2 \mu\text{m}$  and  $0.9 \pm 0.2 \mu\text{m}$  respectively for MCO and 10FeMCO\_R1000 coated Crofer 22 APU.

On the contrary, the thermally-grown oxide scale on coated AISI 441 samples (marked in dashed line in Figure 2 c and d) presents regular depth, being overall thicker compared to the other steel substrate. An estimation of the average thickness has been made by EDX line-scans (not reported here), finding a chromia scale of  $2.1 \pm 0.2 \mu\text{m}$  for all AISI 441 samples. Moreover, the AISI 441 steel surface presents various oxides in the sub-scale area, as it is visible in Figure 2 d (representative for all AISI 441 samples).

The calculated values of the mean porosity of the studied coatings show distinct tendencies among the two substrates. For MCO and 10FeMCO\_R1000 on Crofer 22 APU similar results were found,  $15 \pm 3 \%$ . A common feature of all Crofer 22 APU coated samples is the presence of a densified layer in the coating area alongside the oxide scale interface; the outward part of the coating preserved a greater porosity instead. The difference between the two areas of the coating seems to be more evident with Fe-doping. When the dense area is not considered, the mean porosity becomes  $20 \pm 4 \%$  for MCO and  $17 \pm 4 \%$  for 10FeMCO\_R1000.

Concerning AISI 441 samples, mean porosities are  $21 \pm 2 \%$  for MCO and  $9 \pm 2 \%$  for 10FeMCO\_R1000. Both pristine and Fe-doped MCO coating on AISI 441 do not show any clear densified area after the oxide scale, i.e. the pores of the coating reach the  $\text{Cr}_2\text{O}_3$ -rich scale. Indeed, even if the morphology of MCO coating on the two steel substrates could seem fairly similar at the first glance, the calculated mean porosity values differ of around 6 %. The 10FeMCO\_R1000 coating on AISI 441 exhibits greater densification through the whole thickness and pores coalescence compared to the corresponding one Crofer 22 APU. ~~Considering that the coating on the two samples have the same composition and underwent the same sintering treatment, it is evident that the difference in terms of morphology has to be related to the coating interaction with the two different steel substrates.~~

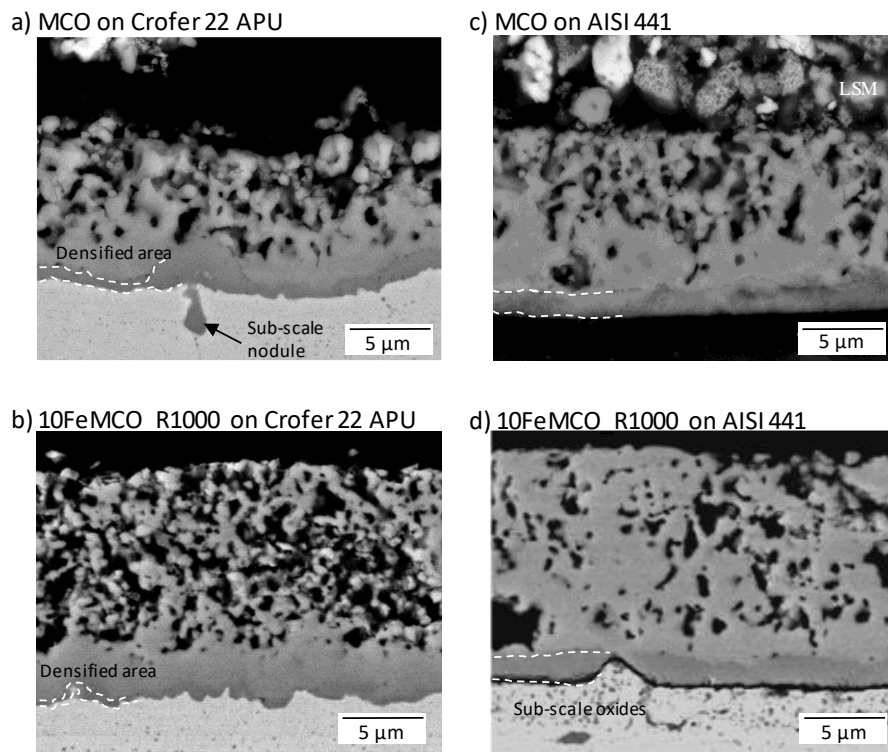


Figure 2: Cross section FE-SEM (backscattered electron mode) images of different coatings after 3200 h at 750°C under a current density of  $0.5 \text{ Acm}^{-2}$ . a) MCO and b) 10FeMCO\_R100 on Crofer 22 APU. c) MCO and d) 10FeMCO\_R1000 on AISI 441.

### 3.3 TEM study on Fe-doped coatings after ASR tests

A more detailed study of the morphology and composition of Fe-doped coatings on Crofer 22 APU and AISI 441 after ASR tests was conducted by transmission electron microscopy (TEM) methods, supported by STEM-EDX and SAED analysis. Results of 10FeMCO\_R1000 coating on Crofer 22 APU substrate are reported in Figure

3; quantification results of marked areas and points are presented in Table 2 and Table 3 respectively. ~~A first inspection of the EDX maps in the figure reveals that two layers of different composition can be distinguished between the Crofer 22 APU and the coating. First, the~~ The Cr map (Figure 3 c) shows that a 0.5 - 1.2  $\mu\text{m}$  thick Cr-rich layer grew as a result of the high-temperature oxidation. The definition of a more precise thickness value is difficult due to uneven edges of the scale; the mean width estimated by various measurements in different areas of these samples is 0.9  $\mu\text{m}$ . EDX analysis on this region (Table 2, area 1) revealed that the composition of the scale is  $\text{Cr}_2\text{O}_3$ , with only trace amount ( $< 0.5$  at. %) of Mn, Co and Fe.

Fe, Cr, Co and Mn maps in Figure 3 reveal that a 1.0 - 1.5  $\mu\text{m}$  reaction layer developed between the  $\text{Cr}_2\text{O}_3$ -scale and the coating as a result of the inter-diffusion of these elements. The microstructure of the reaction layer can be better appreciated in Figure 3 g: it can be recognized for the presence of trapezoidal structures that contain lamellar grains. No signs of delamination or cracking at the interface can be detected, despite the different microstructures of the involved phases. Concerning TEM and SAED investigation on 10FeMCO\_R1000 coated Crofer 22 APU sample, Table 2 (area 2 in Figure 3a) shows that the reaction layer consists of a mixed spinel of Co, Mn and Cr in nearly equimolar amounts; iron is detected in the reaction layer as well, even if in lower concentration (3.4 at. %) compared to the outer part of the coating (5.2 at. %) where the stoichiometric composition is preserved. As shown in the Cr map and by the EDX point analysis reported in Table 3, chromium concentration follows a concentration gradient: indeed, in points 4-7 the Cr concentration varies from 24.2 to 0.9 at. %, while the Co, Mn and Fe concentrations follow opposite trends. The SAED analysis of point 5 (reported in Figure 3 h), matches with the  $\text{CrMnCoO}_4$  tetragonal phase, in agreement with the fact that Co, Mn and Cr are present in very similar quantities.

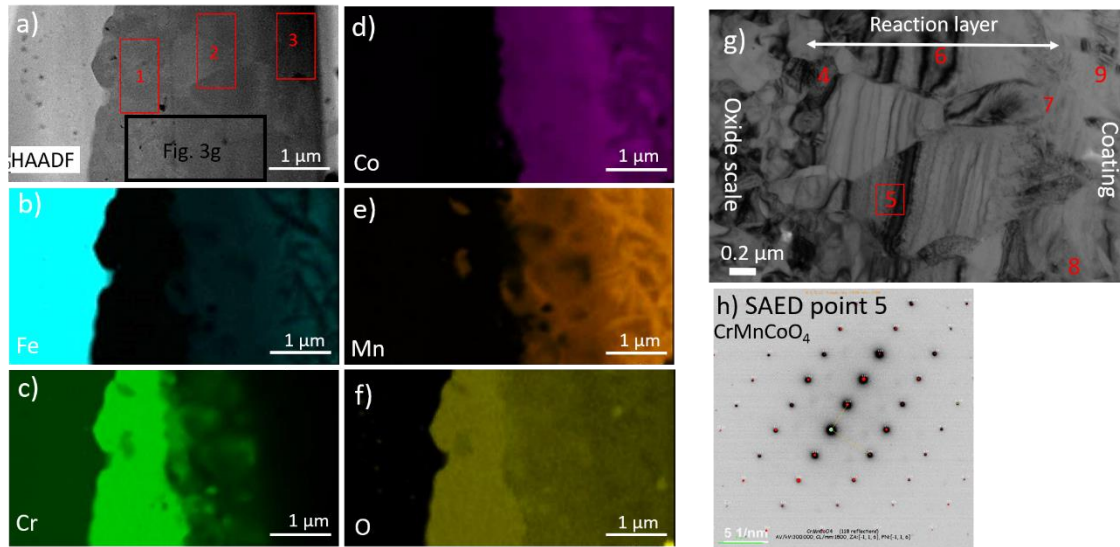


Figure 3: Transmission electron microscopy images of 10FeMCO\_R1000 / Crofer 22 APU FIB lamella: HAADF image with EDX elemental analysis (a-f); BF TEM image (g) with SAED indexed analysis of point 5 (h). Composition of marked areas and points is given in Table 2 and Table 3.

EDX	Co	Mn	Fe	Cr	O	
AREA	At.%	At.%	At.%	At.%	At.%	Area
1	0.3	0.5	0.2	37.8	61.2	Chromium oxide
2	15.6	13.6	3.4	11.1	56.3	Reaction layer
3	14.8	25.7	5.2	0.6	53.7	Coating

Table 2: Results of EDX semi-quantitative analyses collected on marked areas in Figure 3 a.

EDX	Co	Mn	Fe	Cr	O	Calculated
POINT	At.%	At.%	At.%	At.%	At.%	Composition
4	13.4	5.5	1.2	24.2	55.7	$\text{Mn}_{0.4}\text{Co}_{0.9}\text{Fe}_{0.1}\text{Cr}_{1.6}\text{O}_4$
5	15.8	12.8	5.9	11.6	53.9	$\text{Mn}_{0.8}\text{Co}_{1.0}\text{Fe}_{0.4}\text{Cr}_{0.4}\text{O}_4$
6	17.7	17.6	4.1	9.9	50.7	$\text{Mn}_{1.1}\text{Co}_{1.1}\text{Fe}_{0.3}\text{Cr}_{0.6}\text{O}_4$
7	18.0	17.8	7.1	0.9	56.2	$\text{Mn}_{1.2}\text{Co}_{1.2}\text{Fe}_{0.5}\text{Cr}_{0.1}\text{O}_4$

Table 3: Results of EDX semi-quantitative analyses collected on marked points in Figure 4 g. The spinel compositions are calculated on the base of cations fractions, assuming the coatings are stoichiometric spinel oxides.

Figure 4 shows a TEM image with STEM-EDX elemental maps of the 10FeMCO\_R1000 / AISI 441 FIB lamella.

It is apparent from these data that silicon (Figure 4 b) diffused toward the steel surface during the test at 750

°C, forming a non-continuous layer of silicon oxide in the sub-scale region. Also titanium oxide (Figure 4 c) was found to be concentrated **beneath** the steel interface.

Chromium (Figure 4 e) diffused from the AISI 441 and formed a 1.5 - 2.0  $\mu\text{m}$  oxide scale. The manganese concentration in the  $\text{Cr}_2\text{O}_3$  scale formed on AISI 441 (visible in Figure 4 f as well) is significantly higher than for coated Crofer 22 APU (Figure 3). A further difference between coated AISI 441 and Crofer 22 APU samples is the complete absence of any transition layer/phase between the oxide scale and the coating; Cr appeared to be absolutely confined in the scale, not showing a concentration gradient towards the coating side (where only Mn, Co and Fe were detected). This is better presented in Figure 4 i, where a bright-field TEM image of the scale/coating interface is shown; EDX analysis was performed on marked points and reported in Table 4, whereas SAED results are respectively presented in Figure 4 j, k and l. As it is shown, the room -temperature structure of the oxide scale (points 1 and 2) can be described as mixture of pure  $\text{Cr}_2\text{O}_3$  and Mn-Cr mixed oxide; the electrical conductivity of the second phase can be one or two orders of magnitude higher than the former [35]. The comparison of SAED spectra reveals that Mn amount in point 2 caused a distortion of the  $\text{Cr}_2\text{O}_3$  lattice, compared to SAED of point 1. On the other hand, in point 3, taken from the coating close to the oxide scale, only a small amount of Cr was detected. The calculated composition of point 3 based on EDX cations fractions is  $\text{Mn}_{1.2}\text{Co}_{1.4}\text{Fe}_{0.3}\text{Cr}_{0.1}\text{O}_4$ , which is very similar to the nominal composition of the coating; the same structure is confirmed by SAED investigation on this point (Figure 4 l). This data suggests that the Fe-doped coating is effectively limiting the Cr diffusion and consequently the evaporation.

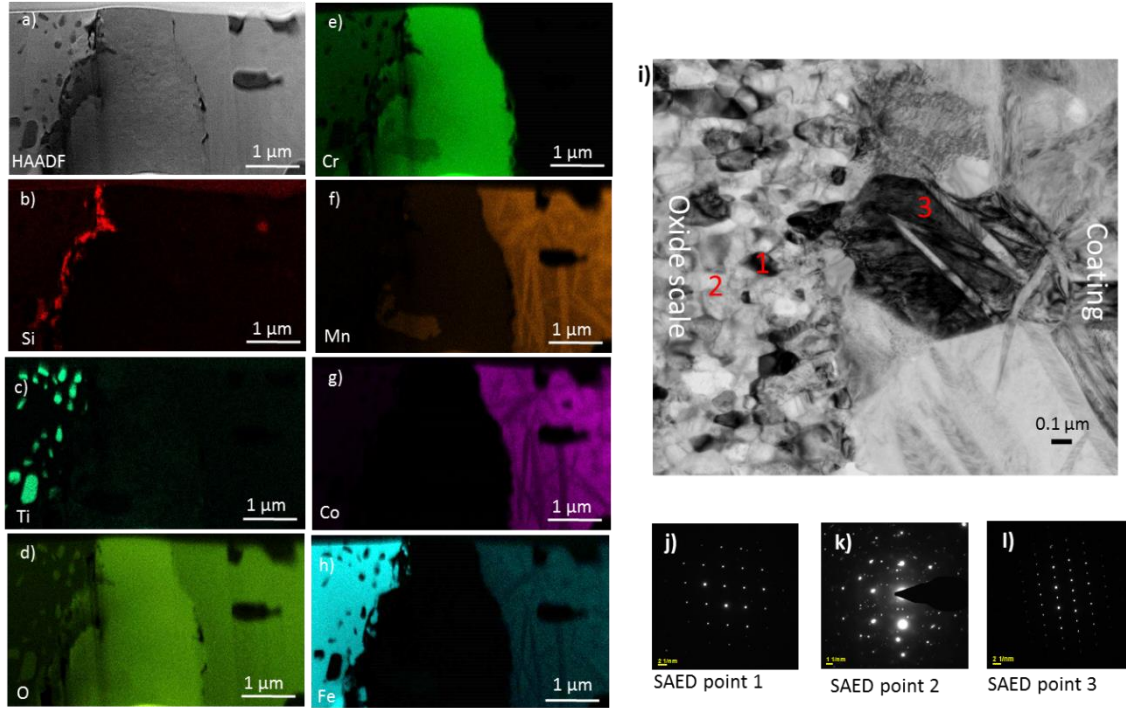


Figure 4: Transmission electron microscopy images of 10FeMCO\_R1000 / AISI441 FIB lamella: HAADF image with EDX elemental analysis (a-h); BF TEM image (i) with SAED analysis of point 1-3 (j-l). Composition of marked points is given in Table 4.

EDX	Co	Mn	Fe	Cr	O
point	At.%	At.%	At.%	At.%	At.%
1	0.1	-	-	32.9	66.9
2	-	5.6	-	24.4	70.0
3	18.5	15.7	4.2	1.4	60.2

Table 4: Results of EDX semi-quantitative analyses collected on marked points in Figure 4 i.

A magnification of the previous FIB lamella, focused on the coating outer area, is reported in Figure 5; it is representative for the Fe-doped coating on Crofer 22 APU as well. The STEM-EDX maps (a-d) demonstrate that both the microstructure and the composition are not homogeneous, but exhibit variable elemental concentrations. ~~However, it is remarked that this structure formed during the cooling of the ASP rig, thus it differs from the high temperature microstructure. Indeed,  $Mn_{1.5}Co_{1.5}O_4$  is known to undergo a phase transition from a cubic to a less conductive mixed cubic tetragonal structure at between 550–450 °C; this has been previously well described for the  $Mn_{1.5}Co_{1.5}O_4$  composition [12,36].~~ Looking at Figure 5 b, it can be observed that Mn concentration is higher in some thin elongated grains that surround broader areas where



Co and Fe presence is higher (see Figure 5 c and d). This is confirmed by EDX analysis and relative calculated compositions reported in Table 5. According to SAED identification (Figure 5 e-g), the larger grains well fit to the  $\text{MnCo}_2\text{O}_4$  spinel (cubic), whereas the elongated grains have been identified as  $\text{Mn}_2\text{CoO}_4$  phase (tetragonal).

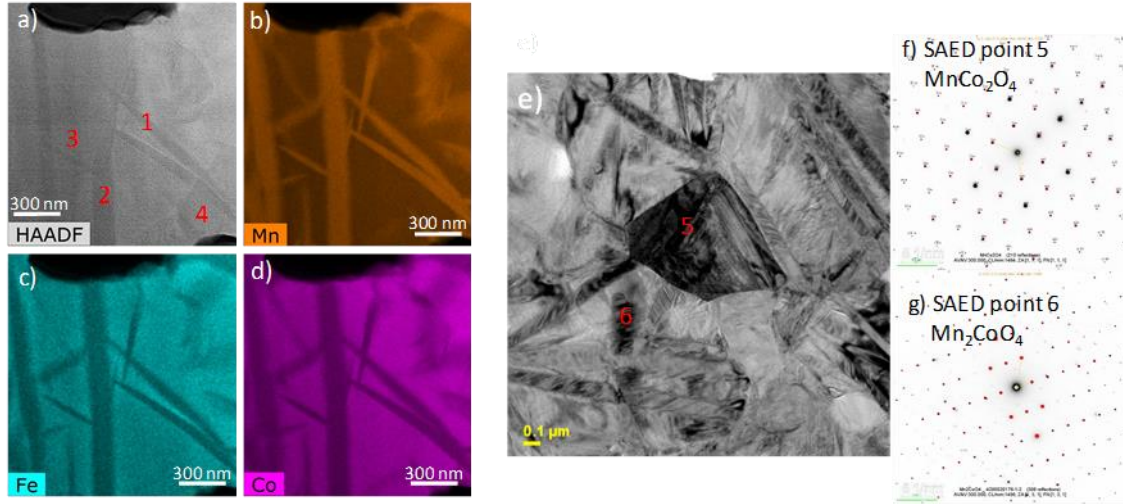


Figure 5: Transmission electron microscopy images of 10FeMCO/AISI 441 FIB lamella: HAADF image with EDX elemental analysis (a-d) and BF TEM image with SAED indexed analysis of point 5 and 6 (e-g). Composition of marked points is given in Table 5.

EDX	Co	Mn	Fe	O	Calculated
	At.%	At.%	At.%	At.%	composition
1	10.3	19.4	1.7	68.6	$\text{Mn}_{1.9}\text{Co}_{1.0}\text{Fe}_{0.2}\text{O}_4$
2	10.0	19.4	2.0	68.6	$\text{Mn}_{1.9}\text{Co}_{1.0}\text{Fe}_{0.2}\text{O}_4$
3	18.7	13.0	2.5	65.8	$\text{Mn}_{1.1}\text{Co}_{1.6}\text{Fe}_{0.2}\text{O}_4$
4	15.5	12.7	3.7	68.1	$\text{Mn}_{1.2}\text{Co}_{1.5}\text{Fe}_{0.3}\text{O}_4$
5	23.7	14.0	2.2	60.1	$\text{Mn}_{1.0}\text{Co}_{1.8}\text{Fe}_{0.2}\text{O}_4$
6	13.6	26.6	0.6	59.2	$\text{Mn}_{2.0}\text{Co}_{1.0}\text{O}_4$

Table 5: Results of EDX semi-quantitative analyses collected on marked points in Figure 5. The spinel compositions are calculated on the base of cations fractions, assuming the coatings are stoichiometric spinel oxides.

### 3.4 Fuel cell test

Two fuel cells were measured in this study: one without any Cr source (with ceramic contact plate – reference measurement) and one with the 10FeMCO\_R1000 coating on Crofer 22 APU interconnect close to the



cathode electrode. Initial performance of the cells was very similar, maximum power density of both cells was  $660 \text{ mW cm}^{-2}$  (obtained at 540 mV) at  $750^\circ\text{C}$ . For the aging experiment, the fuel cell was operated initially at  $0.25 \text{ A cm}^{-2}$  load and then at  $0.5 \text{ A cm}^{-2}$  load, for a total of 200 hours. Results are presented in Figure 6 A. Cells have shown basically the same electrical and electrochemical performance over time. Visible degradation was observed, but as it was similar in both cases. As a results, the presence of the coated alloy does not induce any additional degradation, therefore the coating serves its designed protective role. For the  $0.5 \text{ A cm}^{-2}$  current load, cell voltage dropped from the initial  $\approx 0.84 \text{ V}$  to  $\approx 0.80 \text{ V}$  over  $\approx 200$  hours. Maximum power after the aging occurs for the same voltage and is  $\approx 625 \text{ mW cm}^{-2}$ . Measured impedance spectra (at OCV) show a slight increase of the ohmic resistance (from the initial  $242 \text{ m}\Omega \text{ cm}^2$  to  $265 \text{ m}\Omega \text{ cm}^2$ ) and changes in the impedance part. The higher frequency (HF, peak frequency  $\approx 800 \text{ Hz}$ ) semicircle seems to first decrease between the 0 h and 45 h measurements (from  $\approx 170$  to  $\approx 130 \text{ m}\Omega \text{ cm}^2$ ) and then increase over time ( $\approx 205 \text{ m}\Omega \text{ cm}^2$  after 175 hours), whereas the medium frequency (MF,  $\approx 20 \text{ Hz}$ ) contribution remains unchanged ( $310\text{-}330 \text{ m}\Omega \text{ cm}^2$ ). The lowest frequency (LF,  $\approx 0.2 \text{ Hz}$ ) contribution originates due to gas diffusion and remains constant. We postulate that the HF contribution comes from the hydrogen electrode, which is consistent with the available literature data, pointing to a charge transfer reaction between the Ni and YSZ [37,38]. Our other tests (not shown here) confirm degradation of the used hydrogen electrode due to coarsening of nickel, which stops after  $\approx 600$  hours. The MF contribution comes most probably from the oxygen electrode. The presence of coated interconnect does not influence the degradation rate, therefore the potential electrochemical/chemical poisoning of the cell by Cr species is negligible. Though the test was relatively short, previously published reports concluded that the potential Cr poisoning, if present, is very noticeable in the first hours [39,40]. Yang et al. [40] have shown that the cell in contact with not-coated interconnect degrades very fast in the first 100 hours of operation. Power density decreased from  $0.4 \text{ W cm}^{-2}$  to  $0.15 \text{ W cm}^{-2}$  after only 100 hours. The cell in contact with coated interconnect has activated and increased its power. Sun et al. have observed very similar effects [39]. To determine whether any Cr could be found in the cathode or in the protective coating, SEM/EDX analysis of the cross sections have been performed.

Results are presented in Figure 6 C-D ~~and in Table 6~~. EDX point scans have been performed across the coating/cathode.

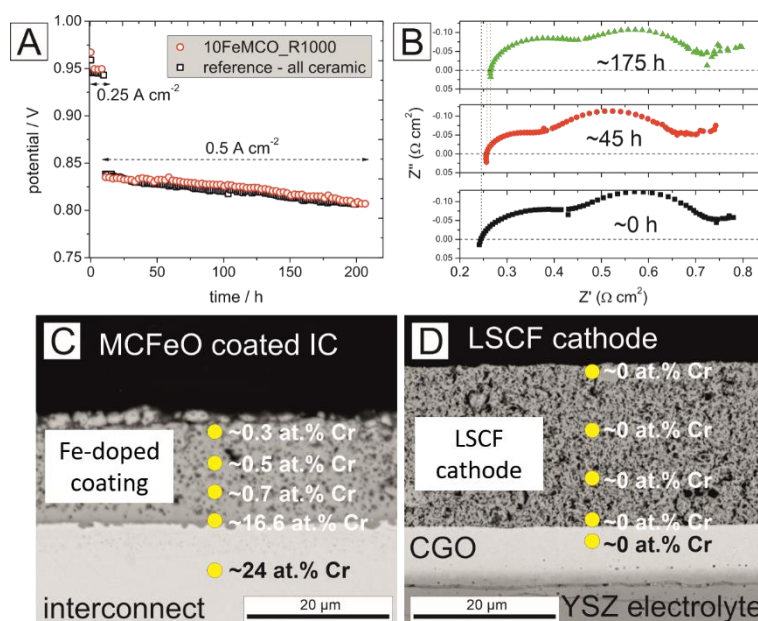


Figure 6: Polarization curve (A) and post mortem SEM analysis of the interconnect (B) and fuel cell cathode (C.) ~~Chemical compositions of the marked points are given in Table 6.~~

Analysis of the interconnect sample with the protective coating after the fuel cell measurement reveals ~~(points B1-B5 in Figure 6 C)~~ minimal amount of Cr (< 1 at. %) that partially might originate from the high temperature sintering step. In the outer layer of the coating ~~(point B1)~~ the amount of Cr is within an experimental error. There is some increasing trend of the Cr content towards the steel/oxide/coating interface. The chemical composition of the coating is as-expected: indeed, calculation of the coating composition (based on EDX cations fractions) confirm what discussed in Section 3.1. Analysis of the LSCF cathode shows no clear peaks from chromium, though its analysis might be subjected to an error caused by overlapping peaks. Additional surface SEM/EDX analysis (not shown here) was in-line with the cross-section study, i.e. the amount of Cr was negligible; the coating has performed its protective role during the fuel cell measurement.

---

~~10FeMCO\_R1000-coating (Figure 6 C)~~

Point/element:	Mn	Co	Fe	Cr	O	Coating composition		
B1—coating	22.59	20.64	5.46	0.27	51.03	$Mn_{1.38}Co_{1.26}Fe_{0.33}Cr_{0.02}O_4$		
B2—coating	23.57	21.16	5.87	0.47	48.92	$Mn_{1.38}Co_{1.24}Fe_{0.34}Cr_{0.03}O_4$		
B3—coating	23.61	21.27	5.83	0.71	48.58	$Mn_{1.38}Co_{1.24}Fe_{0.34}Cr_{0.04}O_4$		
B4—interface	13.73	14.51	10.94	16.56	44.27			
B5—steel	1.01	1.32	69.82	23.85	4.00			
LSCF cathode (Figure 6-D)								
Point/element:	La	Sr	Co	Fe	Cr	Ce	Gd	O
C1—electrode	11.95	7.89	4.21	16.31	0.01	-	-	59.64
C2—electrode	14.69	8.79	4.92	19.40	0.00	-	-	52.19
C3—electrode	13.37	8.98	4.62	17.75	0.00	-	-	55.29
C4—interface	13.13	7.33	4.21	17.17	0.00	7.69	0.46	50.01
C5—barrier layer	-	-	-	-	-	24.71	3.84	62.28

Table 6: Chemical compositions (measured by EDX) of points presented in Figure 6.

## 4. Discussion

### 4.1 Area Specific Resistance

Different phenomena involved AISI 441 and Crofer 22 APU coated samples during the ASR test, as shown in Figure 1 A and B. In principle, the total ASR of the interconnect can be considered as the sum of different resistances connected in series, as expressed by:

$$ASR_{interconnect} = \rho_{coating} * \tau_{coating} + \rho_{oxide\ scale} * \tau_{oxide\ scale} \quad (2)$$

where,  $\rho$  is the specific resistivity and  $\tau$  is the thickness of each layer. The contribution of the steel substrate is ignored due to its high electrical conductivity, while the most significant contribution to the total ASR is

given by the growing oxide scale (based on  $\text{Cr}_2\text{O}_3$  and/or  $(\text{Mn,Cr})_3\text{O}_4$ ), whose conductivity is at least two orders of magnitude lower than the coating. During high-temperature aging  $\tau_{\text{oxide scale}}$  increases, ~~typically~~ reducing  ~~$\tau_{\text{coating}}$ , as well as  $\tau_{\text{steel}}$~~ ; in this regard, the oxidation kinetics of both Crofer 22 APU and AISI 441 have already proved to follow a parabolic law [29,33]. The evidence that coated AISI 441 samples settles to an almost constant resistance value after the completion of the sintering of the LSM contact, despite the growth of a  $> 2 \mu\text{m}$  oxide scale, is a clear evidence of a gradual decrease of  $\rho_{\text{oxide scale}}$ . The reason for this is ascribed to the Mn enrichment of the scale, that can significantly improve the electrical conductivity of the scale compared to pure chromia [41,42].

On the other hand, the ASR increase of coated Crofer 22 APU has to be related to the growth of a poor conductive phase between the coating and the oxide scale, already identified in Sec. 3.3 as reaction layer (RL). To this purpose, several studies have already reported that MCO deposited on Crofer 22 APU interacts with the chromia scale during high-temperature oxidation, developing an intermediate phase; it is due to the inter-diffusion of Cr, Mn and Co elements from the oxide scale and the coating and consists of  $(\text{Mn,Co,Cr})_3\text{O}_4$  spinel [43,44]. The thickness of the RL becomes significant only after long-term tests; indeed, no evident proof of it was found when the oxidation kinetic of the same systems was tested for 2000 h at  $750^\circ\text{C}$  [29]. The electrical conductivity of the reaction layer ranges from that of chromia and the coating, as it gradually decreases by increasing Cr concentration [44,45]. On this basis, expression (2) needs to be modified for coated Crofer 22 APU to:

$$ASR_{\text{interconnect}} = \rho_{\text{coating}} * \tau_{\text{coating}} + \rho_{\text{oxide scale}} * \tau_{\text{oxide scale}} + \rho_{\text{RL}} * \tau_{\text{RL}} \quad (3)$$

According to the calculated degradation rates ( $0.92$  and  $1.70 \text{ m}\Omega \text{ cm}^2/1000 \text{ h}$  for MCO and  $10\text{FeMCO\_R1000}$  coating respectively), it could be argued that ASR of coated Crofer 22 APU samples will constantly increase, following linear trends. Nevertheless, ~~we have already proved that the oxidation kinetic of Crofer 22 APU coated with the same coatings follows a parabolic law [29]; moreover~~ in a recent article of Talic et al. [46] the growth of the reaction layer of MCO and Fe-doped MCO coatings on Crofer 22 APU was proved to be parabolic as well. These evidences suggest that the ASR increase due to both chromia and/or reaction layer

development will not follow a linear trend for MCO and 10FeMCO\_R1000 coated Crofer 22 APU interconnects, but a parabolic one.

Although the area specific resistance of the Fe-doped coating on Crofer 22 APU was slightly lower than for the MCO coating at the end of the test, its degradation rate was found to be significantly higher. In reference to equation (5), it is apparent that iron doping brought to either the growth of a thicker and/or less conductive RL. According to the microscopy results of the present study, any clear difference between the thickness of MCO and Fe-doped MCO reaction layers could be accurately determined. ~~Moreover, previous studies have shown that Fe-doped MCO coatings develop a thinner reaction layer than the pristine spinel [21,44].~~ As reported in Table 2, the Fe content in the RL is on average 3.4 at. %, with a Co/Mn/Fe ratio that is fairly approximable to that of the nominal composition of the coating; the EDX point analysis (Table 3) also shows that the iron amount can be even higher in some zones. This result is particularly interesting, as the remarkable Fe concentration in the reaction layer could be the reason for ASR increase and the higher degradation rate compared to pristine MCO coating. No previous research has reported on a similar RL composition; Talic et al. [46] found around 1 at. % of iron in the RL formed after annealing at 900°C of similar Fe-doped coating.

~~Finally, it is noted that Fe-doping brought to an improvement of the absolute value of ASR compared to pristine MCO coating. This result is in agreement with our earlier observations, which showed that the iron doping of the MCO spinel brings to the development of a thinner oxide scale; this positive effect is further promoted by the higher temperature of the reducing step [29]. Interestingly, the beneficial effect due to Fe-doping is here confirmed not only for Crofer 22 APU but also for AISI 441 substrate (although SEM and TEM investigation did not reveal different oxide scale thickness for pristine and Fe-doped samples in the second case).~~

#### 4.2 Coated Crofer 22 APU: evolution of microstructural and compositional properties at 750°C

Crofer 22 APU samples coated by pristine or Fe-doped coatings (Figure 2 a, b and Figure 3) exhibit two main differences related to the sub-scale nodules and the oxide scale thickness.

The formation of Mn-Cr mixed oxides in the sub-scale region of MCO coated Crofer 22 APU is widely reported in the literature [21,25,43]. As for the growth of the chromia layer, the development of the mixed Mn-Cr spinel is regulated by the inward transport of oxygen and outward diffusion of metallic cations through grain boundaries, where they preferentially form [47]: since the nodules are positioned in the subscale area, it is indicated that the first mechanism is the predominant one. This evidence agrees with the fact that the oxygen partial pressure required for the formation of Mn-Cr spinel is lower than for  $\text{Cr}_2\text{O}_3$ . TEM investigation has revealed that small Mn-rich grains are also present in the sub-scale region 10FeMCO\_R1000 coated samples (Figure 3 e); in agreement with what we have already discussed in [29], the higher temperature of the reducing treatment caused a pre-oxidation of the steel, promoting both the increase of the grain size and the reduction of the preferential sites for outward/inward ions diffusion [48]. However, the lower degree of internal oxidation gives further explanation to the lower ASR values for Fe-doped coating with Crofer 22 APU substrate.

On the other hand, the oxide scale results well adherent to the substrate on all coated Crofer 22 APU samples. In this regard, the minor addition of La to the alloy confirms to be a key element. Indeed, rare earth elements (La, Y, Ce) are generally added in small amounts (0.1-0.2 %) to the special alloys for interconnects, as they have been demonstrated to improve the adhesion of the oxide scale and to decrease the oxidation rate [42,49]. In particular La can modify the predominant diffusion mechanism of vacancies in the chromia scale, from chromium outward diffusion to oxygen inward diffusion [42,50]. Uneven edges of the steel/oxide scale interface (Figure 2 a and b) seem to confirm that oxidation proceeds in the inward direction.

The major evidence is that Fe-doped coating led to the development of a thinner oxide scale compared to pristine MCO. A first explanation is that the higher temperature of the reducing step (1000 °C instead of 900 °C) promoted coating densification, effectively reducing the oxygen partial pressure at the steel interface. However, we have already shown that when the Fe-doped coatings are reduced at 900 °C the oxide scale developed during aging is thinner than that of pure MCO [29]. Therefore, the reason should be found in the microstructure of the Fe-modified MCO spinel. Literature reports that  $\text{Fe}^{3+}$  cations preferentially occupy octahedral sites of the spinel structure; also  $\text{Mn}^{2+/3+}$  cations exhibit the same tendency, while the tetrahedral

sites are mostly occupied by  $\text{Co}^{2+}$  cations [22,23,30]. Therefore, iron and manganese compete to occupy the same sites. A careful analysis of EDX analysis results reported in Table 5 can confirm the same observation, as the Fe and Mn relative amounts in different grains follow opposite trends. Similarly to iron cations,  $\text{Cr}^{3+}$  have a strong preference for octahedral sites and are reported to stabilize the cubic structure as well [68]. It is suggested that the tendency of both Cr and Fe cations to occupy similar positions in the spinel lattice have a positive effect in blocking further chromium diffusion.

This hypothesis matches with EDX results reported in Table 3., ~~where it is demonstrated that in the area of the reaction layer closest to the oxide scale (point 4) a higher amount of Cr is associated with that of Co, whereas Mn and Fe concentrations are low. While shifting towards the coating side (points 5 to 7), Cr decreases together with the increase of Fe and Mn.~~

The progressive compositional variation from chromia to the coating made possible by the RL is here considered a key element to avoid the formation of cracks due to TEC mismatch between the involved phases. Moreover, the reaction layer is beneficial for the oxidation resistance of the interconnect, as it effectively reduces the oxygen partial pressure at the scale/coating interface [43,51]. ~~Our results agree with this observation, as the composition of the coating (Table 2, area 3) in the area close to the reaction layer presents only negligible trace amount of Cr.~~

#### 4.3 Coated AISI 441: evolution of microstructural and compositional properties at 750°C

SEM and TEM investigations of coated AISI 441 samples revealed the presence of Si and Ti sub-scale oxides, as it is visible in Figure 2 d (representative for all AISI 441 samples). The formation of silica is particularly detrimental for both the electrical conductivity and adhesion of the scale [52,53]. ~~Indeed, silica resistivity is the range of  $10^{15}$ - $10^{17} \cdot \Omega \cdot \text{cm}$  [54] and reported TECs are between  $0.5$  and  $5.8 \cdot 10^{-6} \cdot \text{K}^{-1}$  [55].~~

~~While Crofer 22 APU is processed by costly vacuum assisted melting technique to minimise the Si concentration, an alternative approach to hinder the  $\text{SiO}_2$  formation is to add Nb to the steel, causing the precipitation of the  $\text{Fe}_2\text{Nb}$  intermetallic compound (known as Laves phase) that has been reported to partially block Si diffusion [52-53].~~ In the present study, evidences suggest that the Nb addition in the AISI 441 alloy

(0.4 wt. %) is not completely effective in preventing the development of the Si-rich phase. However, it is apparent that ASR was not negatively affected. Figure 4 b shows that the silica does not form a continuous layer; therefore, considering the much higher electrical conductivity of the steel surrounding the silica particles, the remaining pathways could be enough to ensure a sufficient electrical conduction.

Nevertheless, the presence of the mentioned internal oxidation is believed to have a great impact on the diffusion of metallic cations from the steel. Indeed, grain boundaries act as fast diffusion paths for transition metals [33]; it is evident that the presence of such secondary phases increased the extension of grain boundaries compared to the original alloy, allowing ions to diffuse easily. The absence of rare earth elements in the AISI 441 composition gives additional support to the enhanced chromium diffusion from the steel.

The last observations find confirmation in the SEM and TEM results of coated AISI 441 samples (Figure 2 c, d and Figure 4). The thickness of Cr-oxide scale of coated AISI 441 (on average more than double that of Crofer 22 APU), its morphology, as well as the weak substrate/scale interface prove that the mechanism for the oxide scale growth of AISI 441 is dominated by outward diffusion of cations, rather than oxygen inward diffusion. Moreover, the significant Mn enrichment of the oxide scale, together with the absence of sub-scale nodules, give further confirmation to the proposed mechanism.

In this regard, it is reminded that the high-temperature conductivity of  $\text{Cr}_2\text{O}_3$  is strongly influenced by the presence of lattice defects. Many studies reported that the conductivity of the oxide scale can be moderately improved thanks to a slight diffusion of elements from the steel into the scale, where they act as dopant elements; the major positive effect was attributed to Mn but also Ti and Ni [44,54–58]. It is believed that the diffusion of few ppm of Ti, Si or Ni cations can statistically occur during aging, leading to an additional enhancement of the chromia conductivity despite the considerable thickness of the scale. **Therefore, the different composition of the two steels have influence on diffusion mechanisms at the interfaces between the steel and coating.**

Additional considerations are required to examine the effect of the Fe-doped coating on AISI 441 alloy; due to the intensity of cations outward diffusion, the mechanism proposed for coated Crofer 22 APU cannot be



validated for this substrate. Fe-doping apparently led to a marked densification on the whole coating thickness. This suggest that the iron containing spinel has higher reactivity with oxygen and cations diffusing either from the steel or LSM contact.

~~As reported in Figure 4 and 6, it is evident that Cr was confined in the oxide scale. Nonetheless, small voids at the oxide scale/coating interface are visible in the FIB lamella (Figure 4 a): for this reason is not possible to completely exclude that some Cr evaporation phenomena are likely to occur.~~

~~To summarize, the better ASR trend shown by AISI 441 coated samples can be explained by both the doping effect of the oxide scale and the absence of the reaction layer. Nevertheless, the discussed issues related to weak interfaces (first of all, the silica/chromia) suggest that coated AISI 441 could not be suitable as interconnect steel neither with a MCO coating nor with Fe-doped MCO coating.~~

#### 4.3 Discussion on different oxidation and diffusion mechanisms at the interfaces

The substantial morphological differences between Crofer 22 APU and AISI 441 oxide scale have to be ascribed to the different alloys composition. Schematics of different mechanism at the steel/oxide scale/coating interfaces are shown in Figure 7 as discussed in Sections 4.2 and 4.3. The area bordered in red in Figure 8 A represents the main mechanisms occurring during the first stage of oxidation for Crofer 22 APU.

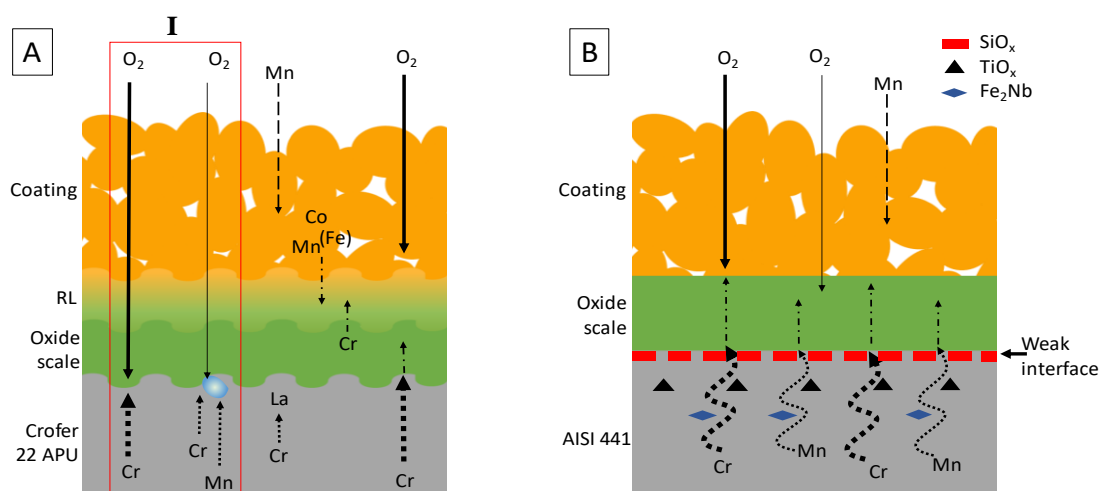


Figure 7: Schematic representation of different mechanism of diffusion, reactivity and oxidation mechanism at the interface during aging at 750°C. A) coated Crofer 22 APU and B) coated AISI 441. (layers thickness not to scale).

~~To summarize, comparing coated AISI 441 with Crofer 22 APU samples showed that the mean degree of difference seems to be the Fe-doping effect on densification and on thickness of the oxide scale. The latter observation may support the hypothesis that ASR behaviour/values could be substantially affected by oxide scale, which gives the most significant contribution to the total ASR.~~

While considering the Crofer 22 APU substrate, a first observation is related to the fact that the 10FeMCO\_R1000 coating both resulted in a thinner oxide scale and reduced the sub scale oxidation. Furthermore, it is interesting that the reaction layer (RL), with negligible traces of Cr, partially replaces the chromia scale; this consequence, together with the positive effect of Fe-doping in reducing the oxide scale growth (and Cr depletion) and promoting the densification of the coating has a beneficial effect in both reducing the contribution to the overall electrical resistivity and minimizing possible CTEs mismatch.

In the case of AISI 441 stainless steel, Ti and Si-based oxides are present in the sub-scale layer; the oxide scale is enriched in Mn, coming from the substrate and contributing to an increase of the electrical conductivity of the oxide scale. One of the issues that emerges from these findings is that a crack developed at the interface between the oxide scale and the Si-rich layer. A further study could assess this behaviour related to dynamic operation effects on the long term resistance and efficacy of the coating, if AISI 441 is used as the interconnect.

Based on the discussed mechanisms, the findings of this research provide insights for the use of  $\text{Mn}_{1.35}\text{Co}_{1.35}\text{Fe}_{0.30}\text{O}_4$  coatings obtained by a simple, versatile and low cost EPD co-deposition method, evaluating and highlighting phenomena taking places by depositing these coatings on different steel substrates with dissimilar oxidation mechanisms.

## 5. Conclusions

This work showed a systematic study of electrical and microstructural properties of Fe-doped MCO spinel as protective coatings for Crofer 22 APU and AISI 441 interconnects. The ASR of 10FeMCO\_R1000 coated substrates demonstrated the lowest resistance values on both Crofer 22 APU and AISI 441 throughout the

test at 750°C. Post mortem investigations revealed that different phenomena occurred for coated Crofer 22 APU and AISI 441 substrates, despite the similar ASR values. The development of a Mn-Co-Cr-Fe reaction layer determined an increase of the ASR for the coated Crofer 22 APU. ~~; however, it is believed that the presence of this intermediate phase is particularly beneficial in terms of blocking Cr depletion. Indeed, cell tests of 10FeMCO\_R1000-coated Crofer 22 APU confirmed positive results both without and with a chromium source.~~ AISI 441 exhibited both a thicker oxide scale and low ASR values; this results can be explained by a doping effect of the scale by minor alloying elements. Despite the absence of a reaction layer, no significant amount of Cr was found in the Fe-doped coating on AISI 441 substrate.

## Acknowledgments

F. S. and A. R. B. would like to acknowledge the funding from KMM-VIN (<http://www.kmm-vin.eu/home/fellowships>) 10<sup>th</sup> call granted to Dr. Antonio Gianfranco Sabato and 11<sup>th</sup> call granted to Elisa Zanchi.

This project has received funding from the European Union's Horizon 2020 research and innovation programme under grant agreement No 823717 – ESTEEM3

## References

- [1] J.W. Fergus, Metallic interconnects for solid oxide fuel cells, *Mater. Sci. Eng. A.* 397 (2005) 271–283. <https://doi.org/10.1016/j.msea.2005.02.047>.
- [2] Z. Yang, Recent advances in metallic interconnects for solid oxide fuel cells, *Int. Mater. Rev.* 53 (2008) 39–54. <https://doi.org/10.1179/174328007X212526>.
- [3] P.D. Jablonski, C.J. Cowen, J.S. Sears, Exploration of alloy 441 chemistry for solid oxide fuel cell interconnect application, *J. Power Sources.* 195 (2010) 813–820. <https://doi.org/10.1016/j.jpowsour.2009.08.023>.

- [4] M.A. Laguna-Bercero, Recent advances in high temperature electrolysis using solid oxide fuel cells: A review, *J. Power Sources*. 203 (2012) 4–16.  
<https://doi.org/10.1016/j.jpowsour.2011.12.019>.
- [5] K. Huang, P.Y. Hou, J.B. Goodenough, Reduced area specific resistance for iron-based metallic interconnects by surface oxide coatings, *Mater. Res. Bull.* 36 (2001) 81–95.  
[https://doi.org/10.1016/S0025-5408\(01\)00506-2](https://doi.org/10.1016/S0025-5408(01)00506-2).
- [6] Z. Yang, M. Guo, N. Wang, C. Ma, J. Wang, M. Han, A short review of cathode poisoning and corrosion in solid oxide fuel cell, *Int. J. Hydrogen Energy*. 42 (2017) 24948–24959.  
<https://doi.org/10.1016/j.ijhydene.2017.08.057>.
- [7] M. Stanislawski, E. Wessel, K. Hilpert, T. Markus, L. Singheiser, Chromium Vaporization from High-Temperature Alloys, *J. Electrochem. Soc.* 154 (2007) A295.  
<https://doi.org/10.1149/1.2434690>.
- [8] H. Falk-Windisch, J.E. Svensson, J. Froitzheim, The effect of temperature on chromium vaporization and oxide scale growth on interconnect steels for Solid Oxide Fuel Cells, *J. Power Sources*. 287 (2015) 25–35. <https://doi.org/10.1016/j.jpowsour.2015.04.040>.
- [9] J.C.W. Mah, A. Muchtar, M.R. Somalu, M.J. Ghazali, Metallic interconnects for solid oxide fuel cell: A review on protective coating and deposition techniques, *Int. J. Hydrogen Energy*. 42 (2017) 9219–9229. <https://doi.org/10.1016/j.ijhydene.2016.03.195>.
- [10] N. Mahato, A. Banerjee, A. Gupta, S. Omar, K. Balani, Progress in material selection for solid oxide fuel cell technology: A review, *Prog. Mater. Sci.* 72 (2015) 141–337.  
<https://doi.org/10.1016/j.pmatsci.2015.01.001>.
- [11] F. Smeacetto, A. De Miranda, S. Cabanas Polo, S. Molin, D. Boccaccini, M. Salvo, A.R. Boccaccini, Electrophoretic deposition of  $\text{Mn}_{1.5}\text{Co}_{1.5}\text{O}_4$  on metallic interconnect and interaction with glass-ceramic sealant for solid oxide fuel cells application, *J. Power Sources*. 280 (2015) 379–386. <https://doi.org/10.1016/j.jpowsour.2015.01.120>.
- [12] M. Bobruk, K. Brylewska, K. Durczak, K. Wojciechowski, A. Adamczyk, T. Brylewski,

Synthesis of manganese-cobalt spinel via wet chemistry methods and its properties, *Ceram. Int.* 43 (2017) 15597–15609. <https://doi.org/10.1016/j.ceramint.2017.08.116>.

- [13] T. Brylewski, W. Kucza, A. Adamczyk, A. Kruk, M. Stygar, M. Bobruk, J. Dąbrowa, Microstructure and electrical properties of  $\text{Mn}_{1+x}\text{Co}_{2-x}\text{O}_4$  ( $0 \leq x \leq 1.5$ ) spinels synthesized using EDTA-gel processes, *Ceram. Int.* 40 (2014) 13873–13882. <https://doi.org/10.1016/j.ceramint.2014.05.106>.
- [14] X. Chen, P.Y. Hou, C.P. Jacobson, S.J. Visco, L.C. De Jonghe, Protective coating on stainless steel interconnect for SOFCs: Oxidation kinetics and electrical properties, *Solid State Ionics*. 176 (2005) 425–433. <https://doi.org/10.1016/j.ssi.2004.10.004>.
- [15] Z. Yang, G.G. Xia, X.H. Li, J.W. Stevenson,  $(\text{Mn},\text{Co})_3\text{O}_4$  spinel coatings on ferritic stainless steels for SOFC interconnect applications, *Int. J. Hydrogen Energy*. 32 (2007) 3648–3654. <https://doi.org/10.1016/j.ijhydene.2006.08.048>.
- [16] L. Chen, E.Y. Sun, J. Yamanis, N. Magdefrau, Oxidation Kinetics of  $\text{Mn}_{1.5}\text{Co}_{1.5}\text{O}_4$ -Coated Haynes 230 and Crofer 22 APU for Solid Oxide Fuel Cell Interconnects, *J. Electrochem. Soc.* 157 (2010) B931. <https://doi.org/10.1149/1.3391820>.
- [17] S. Molin, A.G. Sabato, M. Bindi, P. Leone, G. Cempura, M. Salvo, S. Cabanas Polo, A.R. Boccaccini, F. Smeacetto, Microstructural and electrical characterization of Mn-Co spinel protective coatings for solid oxide cell interconnects, *J. Eur. Ceram. Soc.* 37 (2017) 4781–4791. <https://doi.org/10.1016/j.jeurceramsoc.2017.07.011>.
- [18] S.-I. Lee, J. Hong, H. Kim, J.-W. Son, J.-H. Lee, B.-K. Kim, H.-W. Lee, K.J. Yoon, Highly Dense Mn-Co Spinel Coating for Protection of Metallic Interconnect of Solid Oxide Fuel Cells, *J. Electrochem. Soc.* 161 (2014) F1389–F1394. <https://doi.org/10.1149/2.0541414jes>.
- [19] A. Kruk, M. Stygar, T. Brylewski, Mn–Co spinel protective–conductive coating on AL453 ferritic stainless steel for IT-SOFC interconnect applications, *J. Solid State Electrochem.* 17 (2013) 993–1003. <https://doi.org/10.1007/s10008-012-1952-8>.
- [20] B. Talic, H. Falk-Windisch, V. Venkatachalam, P.V. Hendriksen, K. Wiik, H.L. Lein, Effect

of coating density on oxidation resistance and Cr vaporization from solid oxide fuel cell interconnects, *J. Power Sources*. 354 (2017) 57–67.

<https://doi.org/10.1016/j.jpowsour.2017.04.023>.

- [21] B. Talic, S. Molin, K. Wiik, P.V. Hendriksen, H.L. Lein, Comparison of iron and copper doped manganese cobalt spinel oxides as protective coatings for solid oxide fuel cell interconnects, *J. Power Sources*. 372 (2017) 145–156.

<https://doi.org/10.1016/j.jpowsour.2017.10.060>.

- [22] B. Talic, P.V. Hendriksen, K. Wiik, H.L. Lein, Thermal expansion and electrical conductivity of Fe and Cu doped  $\text{MnCo}_2\text{O}_4$  spinel, *Solid State Ionics*. 326 (2018) 90–99.

<https://doi.org/10.1016/j.ssi.2018.09.018>.

- [23] A. Masi, M. Bellusci, S.J. McPhail, F. Padella, P. Reale, J.-E. Hong, R. Steinberger-Wilckens, M. Carlini, The effect of chemical composition on high temperature behaviour of Fe and Cu doped Mn-Co spinels, *Ceram. Int.* 43 (2016) 2829–2835.

<https://doi.org/10.1016/j.ceramint.2016.11.135>.

- [24] N. Grünwald, Y.J. Sohn, X. Yin, N.H. Menzler, O. Guillon, R. Vaßen, Microstructure and phase evolution of atmospheric plasma sprayed Mn-Co-Fe oxide protection layers for solid oxide fuel cells, *J. Eur. Ceram. Soc.* 39 (2019) 449–460.

<https://doi.org/10.1016/j.jeurceramsoc.2018.08.027>.

- [25] S. Molin, P. Jasinski, L. Mikkelsen, W. Zhang, M. Chen, P. V. Hendriksen, Low temperature processed  $\text{MnCo}_2\text{O}_4$  and  $\text{MnCo}_{1.8}\text{Fe}_{0.2}\text{O}_4$  as effective protective coatings for solid oxide fuel cell interconnects at 750 °C, *J. Power Sources*. 336 (2016) 408–418.

<https://doi.org/10.1016/j.jpowsour.2016.11.011>.

- [26] J. Puranen, J. Lagerbom, L. Hyvärinen, M. Kylmälahti, O. Himanen, M. Pihlatie, J. Kiviaho, P. Vuoristo, The structure and properties of plasma sprayed iron oxide doped manganese cobalt oxide spinel coatings for SOFC metallic interconnectors, *J. Therm. Spray Technol.* 20 (2011) 154–159. <https://doi.org/10.1007/s11666-010-9598-5>.

- [27] M. Bednarz, S. Molin, M. Bobruk, M. Stygar, E. Długoń, M. Sitarz, T. Brylewski, High-temperature oxidation of the Crofer 22 H ferritic steel with  $\text{Mn}_{1.45}\text{Co}_{1.45}\text{Fe}_{0.1}\text{O}_4$  and  $\text{Mn}_{1.5}\text{Co}_{1.5}\text{O}_4$  spinel coatings under thermal cycling conditions and its properties, *Mater. Chem. Phys.* 225 (2019) 227–238. <https://doi.org/10.1016/j.matchemphys.2018.12.090>.
- [28] A.G. Sabato, S. Molin, H. Javed, E. Zanchi, A.R. Boccaccini, F. Smeacetto, In-situ Cu-doped MnCo-spinel coatings for solid oxide cell interconnects processed by electrophoretic deposition, *Ceram. Int.* 45 (2019) 19148–19157. <https://doi.org/10.1016/j.ceramint.2019.06.161>.
- [29] E. Zanchi, B. Talic, A.G. Sabato, S. Molin, A.R. Boccaccini, F. Smeacetto, Electrophoretic co-deposition of  $\text{Fe}_2\text{O}_3$  and  $\text{Mn}_{1.5}\text{Co}_{1.5}\text{O}_4$ : Processing and oxidation performance of Fe-doped Mn-Co coatings for solid oxide cell interconnects, *J. Eur. Ceram. Soc.* 39 (2019) 3768–3777. <https://doi.org/10.1016/j.jeurceramsoc.2019.05.024>.
- [30] Y. Liu, J.W. Fergus, K. Wang, C. Dela Cruz, Crystal Structure, Chemical Stabilities and Electrical Conductivity of Fe-Doped Manganese Cobalt Spinel Oxides for SOFC Interconnect Coatings, *J. Electrochem. Soc.* 160 (2013) F1316–F1321. <https://doi.org/10.1149/2.114311jes>.
- [31] C.A. Schneider, W.S. Rasband, K.W. Eliceiri, NIH Image to ImageJ: 25 years of image analysis, *Nat. Methods.* 9 (2012) 671–675. <https://doi.org/10.1038/nmeth.2089>.
- [32] V.I. Gorokhovskiy, P.E. Gannon, M.C. Deibert, R.J. Smith, A. Kayani, M. Kopczyk, D. VanVorous, Z. Yang, J.W. Stevenson, S. Visco, C. Jacobson, H. Kurokawa, S.W. Sofie, Deposition and Evaluation of Protective PVD Coatings on Ferritic Stainless Steel SOFC Interconnects, *J. Electrochem. Soc.* 153 (2006) A1886. <https://doi.org/10.1149/1.2266244>.
- [33] Z. Yang, G.G. Xia, C.M. Wang, Z. Nie, J. Templeton, J.W. Stevenson, P. Singh, Investigation of iron-chromium-niobium-titanium ferritic stainless steel for solid oxide fuel cell interconnect applications, *J. Power Sources.* 183 (2008) 660–667. <https://doi.org/10.1016/j.jpowsour.2008.05.037>.

- [34] S. Chandra-Ambhorn, Y. Wouters, L. Antoni, F. Toscan, A. Galerie, Adhesion of oxide scales grown on ferritic stainless steels in solid oxide fuel cells temperature and atmosphere conditions, *J. Power Sources*. 171 (2007) 688–695.  
<https://doi.org/10.1016/j.jpowsour.2007.06.058>.
- [35] Z. Lu, J. Zhu, E. Andrew Payzant, M.P. Paranthaman, Electrical Conductivity of the Manganese Chromite Spinel Solid Solution, *J. Am. Ceram. Soc.* 88 (2005) 1050–1053.  
<https://doi.org/10.1111/j.1551-2916.2005.00205.x>.
- [36] T. Brylewski, A. Kruk, A. Adamczyk, W. Kucza, M. Stygar, K. Przybylski, Synthesis and characterization of the manganese cobaltite spinel prepared using two “soft chemical” methods, *Mater. Chem. Phys.* 137 (2012) 310–316.  
<https://doi.org/10.1016/j.matchemphys.2012.09.026>.
- [37] R. Barfod, A. Hagen, S. Ramousse, P. V. Hendriksen, M. Mogensen, Break Down of Losses in Thin Electrolyte SOFCs, *Fuel Cells*. 6 (2006) 141–145.  
<https://doi.org/10.1002/fuce.200500113>.
- [38] R. Barfod, M. Mogensen, T. Klemensø, A. Hagen, Y.-L. Liu, P. Vang Hendriksen, Detailed Characterization of Anode-Supported SOFCs by Impedance Spectroscopy, *J. Electrochem. Soc.* 154 (2007) B371. <https://doi.org/10.1149/1.2433311>.
- [39] Z. Sun, R. Wang, A.Y. Nikiforov, S. Gopalan, U.B. Pal, S.N. Basu, CuMn<sub>1.8</sub>O<sub>4</sub> protective coatings on metallic interconnects for prevention of Cr-poisoning in solid oxide fuel cells, *J. Power Sources*. 378 (2018) 125–133. <https://doi.org/10.1016/j.jpowsour.2017.12.031>.
- [40] Z. Yang, G. Xia, S.P. Simner, J.W. Stevenson, Thermal Growth and Performance of Manganese Cobaltite Spinel Protection Layers on Ferritic Stainless Steel SOFC Interconnects, *J. Electrochem. Soc.* 152 (2005) A1896. <https://doi.org/10.1149/1.1990462>.
- [41] W. Qu, L. Jian, J.M. Hill, D.G. Ivey, Electrical and microstructural characterization of spinel phases as potential coatings for SOFC metallic interconnects, *J. Power Sources*. 153 (2006) 114–124. <https://doi.org/10.1016/j.jpowsour.2005.03.137>.



- [42] H.S. Seo, G. Jin, J.H. Jun, D.H. Kim, K.Y. Kim, Effect of reactive elements on oxidation behaviour of Fe-22Cr-0.5Mn ferritic stainless steel for a solid oxide fuel cell interconnect, *J. Power Sources*. 178 (2008) 1–8. <https://doi.org/10.1016/j.jpowsour.2007.12.026>.
- [43] N.J. Magdefrau, L. Chen, E.Y. Sun, J. Yamanis, M. Aindow, Formation of spinel reaction layers in manganese cobaltite-coated Crofer22 APU for solid oxide fuel cell interconnects, *J. Power Sources*. 227 (2013) 318–326. <https://doi.org/10.1016/j.jpowsour.2012.07.091>.
- [44] K. Wang, Y. Liu, J.W. Fergus, Interactions between SOFC interconnect coating materials and chromia, *J. Am. Ceram. Soc.* 94 (2011) 4490–4495. <https://doi.org/10.1111/j.1551-2916.2011.04749.x>.
- [45] Y. Liu, J.W. Fergus, C. Dela Cruz, Electrical properties, cation distributions, and thermal expansion of manganese cobalt chromite spinel oxides, *J. Am. Ceram. Soc.* 96 (2013) 1841–1846. <https://doi.org/10.1111/jace.12254>.
- [46] B. Talic, P.V. Hendriksen, K. Wiik, H.L. Lein, Diffusion couple study of the interaction between Cr<sub>2</sub>O<sub>3</sub> and MnCo<sub>2</sub>O<sub>4</sub> doped with Fe and Cu, *Solid State Ionics*. 332 (2019) 16–24. <https://doi.org/10.1016/j.ssi.2019.01.008>.
- [47] N.J. Magdefrau, L. Chen, E.Y. Sun, M. Aindow, Effects of alloy heat treatment on oxidation kinetics and scale morphology for crofer 22 APU, *J. Power Sources*. 241 (2013) 756–767. <https://doi.org/10.1016/j.jpowsour.2013.03.181>.
- [48] B. Talic, S. Molin, P.V. Hendriksen, H.L. Lein, Effect of pre-oxidation on the oxidation resistance of Crofer 22 APU, *Corros. Sci.* 138 (2018) 189–199. <https://doi.org/10.1016/j.corsci.2018.04.016>.
- [49] P.Y. Hou, J. Stringer, The effect of reactive element additions on the selective oxidation, growth and adhesion of chromia scales, *Mater. Sci. Eng. A*. 202 (1995) 1–10. [https://doi.org/10.1016/0921-5093\(95\)09798-8](https://doi.org/10.1016/0921-5093(95)09798-8).
- [50] G. Jalilvand, M.-A.A. Faghihi-Sani, Fe doped Ni–Co spinel protective coating on ferritic stainless steel for SOFC interconnect application, *Int. J. Hydrogen Energy*. 38 (2013) 12007–

12014. <https://doi.org/10.1016/j.ijhydene.2013.06.105>.

- [51] T. Horita, H. Kishimoto, K. Yamaji, Y. Xiong, M.E. Brito, H. Yokokawa, Y. Baba, K. Ogasawara, H. Kameda, Y. Matsuzaki, S. Yamashita, N. Yasuda, T. Uehara, Diffusion of oxygen in the scales of Fe-Cr alloy interconnects and oxide coating layer for solid oxide fuel cells, *Solid State Ionics*. 179 (2008) 2216–2221. <https://doi.org/10.1016/j.ssi.2008.07.024>.
- [52] T. Horita, H. Kishimoto, K. Yamaji, Y. Xiong, N. Sakai, M.E. Brito, H. Yokokawa, Evaluation of Laves-phase forming Fe-Cr alloy for SOFC interconnects in reducing atmosphere, *J. Power Sources*. 176 (2008) 54–61.  
<https://doi.org/10.1016/j.jpowsour.2007.10.041>.
- [53] R. Sachitanand, M. Sattari, J.E. Svensson, J. Froitzheim, Evaluation of the oxidation and Cr evaporation properties of selected FeCr alloys used as SOFC interconnects, *Int. J. Hydrogen Energy*. 38 (2013) 15328–15334. <https://doi.org/10.1016/j.ijhydene.2013.09.044>.
- [54] P.D. Jablonski, D.E. Alman, Oxidation resistance of novel ferritic stainless steels alloyed with titanium for SOFC interconnect applications, *J. Power Sources*. 180 (2008) 433–439.  
<https://doi.org/10.1016/j.jpowsour.2008.02.010>.
- [55] W.J. Quadackers, J. Piron-Abellan, V. Shemet, L. Singheiser, Metallic interconnectors for solid oxide fuel cells – a review, *Mater. High Temp*. 20 (2003) 115–127.  
<https://doi.org/10.1179/mht.2003.015>.
- [56] M. Palcut, L. Mikkelsen, K. Neufeld, M. Chen, R. Knibbe, P. V. Hendriksen, Corrosion stability of ferritic stainless steels for solid oxide electrolyser cell interconnects, *Corros. Sci*. 52 (2010) 3309–3320. <https://doi.org/10.1016/j.corsci.2010.06.006>.
- [57] H. Nagai, T. Fujikawa, K. Shoji, Electrical Conductivity of Cr<sub>2</sub>O<sub>3</sub> Doped with La<sub>2</sub>O<sub>3</sub>, Y<sub>2</sub>O<sub>3</sub> and NiO, *Trans. Japan Inst. Met.* 24 (1983) 581–588.  
<https://doi.org/10.2320/matertrans1960.24.581>.
- [58] H.S. Seo, D.W. Yun, K.Y. Kim, Oxidation behavior of ferritic stainless steel containing Nb, Nb-Si and Nb-Ti for SOFC interconnect, *Int. J. Hydrogen Energy*. 38 (2013) 2432–2442.

<http://doi.org/10.1016/j.ijhydene.2012.12.073>.